
First-in-Human PET Imaging and Estimated Radiation Dosimetry of L-[5-¹¹C]-Glutamine in Patients with Metastatic Colorectal Cancer

Allison S. Cohen^{1,2}, Joe Grudzinski³, Gary T. Smith^{4,5}, Todd E. Peterson^{2,4}, Jennifer G. Whisenant^{6,7}, Tiffany L. Hickman⁷, Kristen K. Ciombor^{6,7}, Dana Cardin^{6,7}, Cathy Eng^{6,7}, Laura W. Goff^{6,7}, Satya Das^{6,7}, Robert J. Coffey^{6,7,8}, Jordan D. Berlin^{6,7}, and H. Charles Manning^{1,2,4,7}

¹Vanderbilt Center for Molecular Probes, Vanderbilt University Medical Center, Nashville, Tennessee; ²Vanderbilt University Institute of Imaging Science, Vanderbilt University Medical Center, Nashville, Tennessee; ³Internal Dosimetry Consultants, LLC, Madison, Wisconsin; ⁴Department of Radiology and Radiological Sciences, Vanderbilt University Medical Center, Nashville, Tennessee; ⁵Section Chief, Nuclear Medicine, Tennessee Valley Healthcare System, Nashville VA Medical Center, Nashville, Tennessee; ⁶Department of Medicine, Vanderbilt University Medical Center, Nashville, Tennessee; ⁷Vanderbilt-Ingram Cancer Center, Vanderbilt University Medical Center, Nashville, Tennessee; and ⁸Department of Cell and Developmental Biology, Vanderbilt University, Nashville, Tennessee

Altered metabolism is a hallmark of cancer. In addition to glucose, glutamine is an important nutrient for cellular growth and proliferation. Non-invasive imaging via PET may help facilitate precision treatment of cancer through patient selection and monitoring of treatment response. L-[5-¹¹C]-glutamine (¹¹C-glutamine) is a PET tracer designed to study glutamine uptake and metabolism. The aim of this first-in-human study was to evaluate the radiologic safety and biodistribution of ¹¹C-glutamine for oncologic PET imaging. **Methods:** Nine patients with confirmed metastatic colorectal cancer underwent PET/CT imaging. Patients received 337.97 ± 44.08 MBq of ¹¹C-glutamine. Dynamic PET acquisitions that were centered over the abdomen or thorax were initiated simultaneously with intravenous tracer administration. After the dynamic acquisition, a whole-body PET/CT scan was acquired. Volume-of-interest analyses were performed to obtain estimates of organ-based absorbed doses of radiation. **Results:** ¹¹C-glutamine was well tolerated in all patients, with no observed safety concerns. The organs with the highest radiation exposure included the bladder, pancreas, and liver. The estimated effective dose was 4.46E-03 ± 7.67E-04 mSv/MBq. Accumulation of ¹¹C-glutamine was elevated and visualized in lung, brain, bone, and liver metastases, suggesting utility for cancer imaging. **Conclusion:** PET using ¹¹C-glutamine appears safe for human use and allows noninvasive visualization of metastatic colon cancer lesions in multiple organs. Further studies are needed to elucidate its potential for other cancers and for monitoring response to treatment.

Key Words: ¹¹C-glutamine; metabolism; PET; colorectal cancer

J Nucl Med 2022; 63:36–43

DOI: 10.2967/jnumed.120.261594

Altered metabolism has been shown to be important for cancer cell growth and proliferation (1,2). Conventional metabolic imaging

has focused primarily on the role of glucose through PET imaging with ¹⁸F-FDG. However, studies have demonstrated the importance of additional metabolic pathways (2–8). This feature of cancer has led to the development of metabolism-targeted imaging and therapeutic strategies focused on pathways other than glycolysis (3–5,7–14). Noninvasive molecular imaging with novel PET tracers is increasingly being deployed in clinical oncology. Targeting tumor-specific pathways represents a promising approach for improved PET imaging of tumors.

Glutamine represents an important metabolic substrate that is dysregulated in cancer (3–9,11–14). Glutamine metabolism allows for energy production via adenosine triphosphate, anaplerosis through the tricarboxylic acid cycle, defense against oxidative stress via glutathione, and biosynthesis of other amino acids and nucleotides (3–9,12). In oncology, glutamine is transported into cells primarily by ASCT2, the sodium-dependent neutral amino acid transporter encoded by *SLC1A5*. ASCT2 is overexpressed in several cancer types (12–14), and this characteristic has been linked to poor survival (13). Imaging of glutamine could be complementary to ¹⁸F-FDG imaging by identifying tumors that either are ¹⁸F-FDG-negative or are in locations with high background ¹⁸F-FDG uptake (7). In addition, glutamine imaging could provide further information about the cancer's underlying biology. Finally, it could serve as a tool for new therapies targeting glutamine metabolism (15,16).

Syntheses of both ¹⁸F- and ¹¹C-labeled glutamine have been reported (17–27). ¹⁸F-glutamine has been studied preclinically (28–39) and clinically (31,36,40–43). However, the distribution and metabolism of ¹⁸F-glutamine differ from those of the naturally occurring substrate, and ¹⁸F-glutamine is prone to defluorination in vivo (28,31,40). L-[5-¹¹C]-glutamine (¹¹C-glutamine) is chemically and biologically identical to physiologic glutamine. Cells that avidly take up glutamine will also avidly take up ¹¹C-glutamine, thereby providing a direct marker of glutamine transport and the first step of glutaminolysis. ¹¹C-glutamine has been studied in preclinical mouse models (21) but to date has not been studied in humans. Here, we report the first-in-human studies using ¹¹C-glutamine in a clinical trial of patients with colorectal cancer.

Received Dec. 23, 2020; revision accepted Mar. 26, 2021.

For correspondence or reprints, contact H. Charles Manning (hcmanning@manderson.org).

Published online Apr. 30, 2021.

COPYRIGHT © 2022 by the Society of Nuclear Medicine and Molecular Imaging.

MATERIALS AND METHODS

Patients

Patients were prospectively enrolled in a clinical trial conducted at Vanderbilt University Medical Center (VUMC, ClinicalTrials.gov identifier NCT03263429) and underwent baseline (pretreatment) PET/CT imaging. The trial was approved by VUMC's Institutional Review Board and all subjects provided written informed consent before participating in the study. The study was conducted in accordance with the Helsinki Declaration and the Health Insurance Portability and Accountability Act. All patients were at least 18 y old, had a histologically or cytologically confirmed diagnosis of metastatic wild-type *KRAS* colorectal cancer, and had received prior antiepidermal growth factor receptor therapy. In addition, patients had undergone baseline evaluation of disease status by CT or MRI and had at least 1 measurable lesion as defined by RECIST 1.1.

¹¹C-Glutamine Production

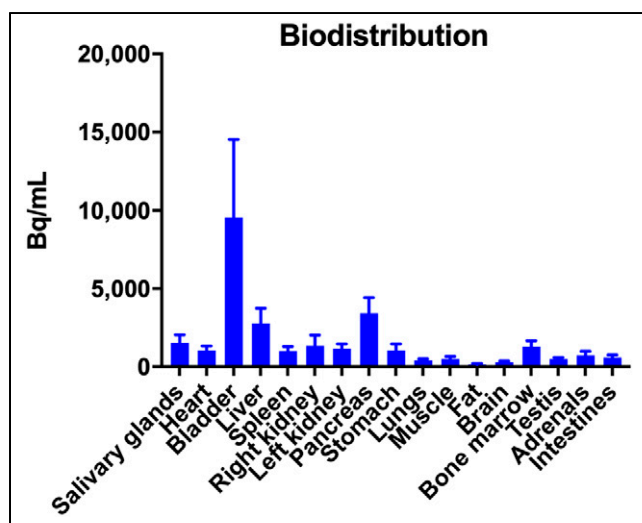
¹¹C-glutamine was synthesized by the VUMC Radiochemistry Core as previously described (27) under current good-manufacturing-practice conditions with approval from the VUMC Radioactive Drug Research Committee. ¹¹C-glutamine met all *U.S. Pharmacopeia* chapter 823 requirements for a sterile, injectable PET radiopharmaceutical. Quality control included analysis of radiochemical and chemical purities, residual solvent content, endotoxin content, pH, filter integrity, radionuclidic purity, and appearance. Sterility testing was performed after release. The production method yields mass levels below 800 μg, which falls several orders of magnitude below reported safe dose levels (44–46). Molar activity was not measured given that these mass levels fall below the detection limit of the instrumentation.

Imaging Protocol

Images were acquired using a Philips Vereos PET/CT scanner with patients lying supine. A dynamic imaging protocol was conducted before a whole-body protocol. Patients were asked to fast for at least 6 h before tracer injection, and blood glucose levels were tested before administration of radioactivity. The PET acquisition was initiated simultaneously with intravenous injection of ¹¹C-glutamine over 30 s. The mean administered activity (±SD) was 337.97 ± 44.08 MBq (range, 232.36–386.98 MBq). Dynamic emission images were acquired over the tumor region of interest using six 1-min scans, six 2-min scans, six 5-min scans, and one 10-min scan, for a total duration of 58 min, as tolerated by the patient. A whole-body (vertex of skull to mid thighs) PET scan was then acquired using 9 bed positions, at 2 min per bed position, for a total scan time of about 18 min. Before and accompanying each PET image exam, a brief low-energy, whole-body transmission CT scan without contrast medium (120 kVp, 25 mAs, and 4.0-mm slice thickness) was acquired for attenuation correction and anatomic localization. PET images were reconstructed using iterative ordered-subset expectation maximization (15 subsets, 3 iterations), with all corrections applied. The reconstructed PET images had a 4-mm slice thickness and a 169 × 169 transaxial matrix with 4-mm pixel spacing. Patients were monitored during and for 24 h after the PET scan for any reactions or adverse events. Side effects and reactions were graded per the Common Terminology Criteria for Adverse Events, version 4.03. There were no adverse or clinically detectable pharmacologic effects in any of the 9 subjects.

Image Analysis

Maximum-intensity-projection and PET/CT images were viewed using OsiriX (Pixmeo). Regions of interest were drawn over lesions, normal liver, and the left ventricular blood pool. The ratios of the maximum value in the lesion to the average value in the blood pool from whole-body images were documented for each lesion for the patients shown in the figures. The ratios of the maximum value in the lesion to the average value in the normal liver from whole-body images



RGB

FIGURE 1. Whole-body biodistribution of ¹¹C-glutamine uptake in normal tissues. Activity concentration (Bq/mL) is plotted for 1 h after injection.

are given for the liver lesions shown in the figures. A volume-of-interest (VOI) analysis was performed for both the dynamic and the whole-body imaging protocols using the Inveon Research Workplace, version 4.2 (Siemens Medical Solutions USA). For analysis of the dynamic PET images, VOIs were drawn over the organs that were within the dynamic PET protocol's field of view, which consisted of 1 bed position and spanned either the lungs or the abdomen. The mean activity concentration (Bq/mL) in each VOI was decay-corrected to the beginning of the study to generate time–activity curves over the duration of the scan. Those patients whose abdomen was within the PET field of view during the dynamic PET protocol were suitable for radiation dosimetry estimation. For the whole-body imaging protocol, VOIs were drawn over organs throughout the entire body. The mean concentration (Bq/mL) and SUV using the patient's body weight were calculated for each VOI.

TABLE 1
Cumulative Activity of ¹¹C-Glutamine in Organs of Interest for Each Patient

Organ	Patient 1	Patient 2	Patient 3
Adrenals	0.00026	0.00016	0.00010
Small intestine	0.00679	0.00493	0.00389
Stomach	0.00256	0.00078	0.00155
Heart	0.00582	0.00424	0.00355
Right kidney	0.00316	0.00427	0.00199
Left kidney	0.00317	0.00372	0.00195
Liver	0.09487	0.06391	0.07328
Pancreas	0.00421	0.00374	0.00302
Bone marrow	0.02184	0.02638	0.01318
Bladder	0.00905	0.01345	0.00856
Total	0.15175	0.12557	0.11106
Remainder	0.33788	0.36405	0.37857

Data are in Bq-h/Bq.

Patient-to-Phantom Data Conversion

To convert patient %ID/g ($[\%ID/g]_{\text{patient}}$) values to phantom whole-organ %ID/organ ($[\%ID/organ]_{\text{phantom}}$) for use in estimating whole-organ cumulative activities, Equation 1 was used:

$$[\%ID/organ]_{\text{phantom}} = [\%ID/g]_{\text{patient}} \cdot TBM_{\text{patient}} \cdot \frac{OM_{\text{phantom}}}{TBM_{\text{phantom}}}, \quad \text{Eq. 1}$$

where TBM_{patient} is the total-body mass of the patient, OM_{phantom} is the phantom organ mass (from the OLINDA organ mass listing (47,48) and Reference Man (49)), and TBM_{phantom} is the phantom total-body mass (adult male, 74 kg; adult female, 57 kg). This approach assumes that the concentration of activity in a tissue relative to the overall concentration in the whole body is preserved when translating from patient to phantom.

Cumulative Activity Calculation

Cumulative activity for each organ was calculated from the biokinetic curves of the dynamic PET scans by first multiplying each point by $e^{-\lambda_{\text{phys}}t}$, where λ_{phys} is the decay constant for ^{11}C , 2.04 h^{-1} , and t is the postinjection time of the data point. Piecewise numeric integration using the trapezoidal method was applied to calculate the cumulative

activity for each organ. The cumulative activity from $t=0, t_0$, to the final time point, $t_f, \tilde{A}_{t_0 \rightarrow t_f}$ (Bq-h), was calculated by numerically integrating the tissue radioactivity using the trapezoidal rule in Equation 2:

$$\tilde{A}_{t_0 \rightarrow t_f} = \int_{t_0}^{t_f} A(t) \approx \sum_{i=t_0}^{t_f-1} (t_{i+1} - t_i) \left(\frac{A(t_{i+1}) + A(t_i)}{2} \right). \quad \text{Eq. 2}$$

The cumulative activity from the time of the final scan time point, t_f , to infinity, $t_{\infty}, \tilde{A}_{t_f \rightarrow t_{\infty}}$ (Bq-h), was calculated by dividing the activity after the final scan, $A(t_f)$, by the physical decay constant, λ_{phys} :

$$\tilde{A}_{t_f \rightarrow t_{\infty}} = \int_{t_f}^{t_{\infty}} A(t) = \int_{t_f}^{t_{\infty}} \exp(-\lambda_{\text{phys}}t) = A(t_f) / \lambda_{\text{phys}}. \quad \text{Eq. 3}$$

The total cumulative activity, $\tilde{A}_{t_0 \rightarrow t_{\infty}}$ (Bq-h), was then calculated by summing $\tilde{A}_{t_0 \rightarrow t_f}$ and $\tilde{A}_{t_f \rightarrow t_{\infty}}$:

$$\tilde{A}_{t_0 \rightarrow t_{\infty}} = \tilde{A}_{t_0 \rightarrow t_f} + \tilde{A}_{t_f \rightarrow t_{\infty}}. \quad \text{Eq. 4}$$

The number of decays per injected activity (Bq-h/Bq) was computed for each organ by dividing the cumulative activity by the injected activity (Bq). Furthermore, the number of decays per injected activity for the remainder was computed by subtracting the sum of organ cumulative

TABLE 2
Dosimetry Estimates for Adults Based on Dynamic PET Imaging with ^{11}C -Glutamine

(mGy/MBq)	Patient 1	Patient 2	Patient 3	Mean	SD	COV (%)
Adrenals	7.51E-03	5.53E-03	3.61E-03	5.55E-03	1.95E-03	35%
Brain	2.47E-03	2.66E-03	2.13E-03	2.42E-03	2.69E-04	11%
Breasts	2.59E-03	2.67E-03	2.15E-03	2.47E-03	2.80E-04	11%
Gallbladder wall	5.44E-03	4.81E-03	4.17E-03	4.81E-03	6.35E-04	13%
Lower large intestine wall	3.42E-03	3.69E-03	2.83E-03	3.31E-03	4.40E-04	13%
Small intestine	5.60E-03	5.08E-03	2.99E-03	4.56E-03	1.38E-03	30%
Stomach wall	5.01E-03	3.94E-03	2.93E-03	3.96E-03	1.04E-03	26%
Upper large intestine wall	3.89E-03	3.87E-03	3.04E-03	3.60E-03	4.85E-04	13%
Heart wall	5.57E-03	4.94E-03	3.90E-03	4.80E-03	8.43E-04	18%
Kidneys	8.27E-03	9.65E-03	5.14E-03	7.69E-03	2.31E-03	30%
Liver	2.21E-02	1.53E-02	1.31E-02	1.68E-02	4.69E-03	28%
Lungs	3.41E-03	3.37E-03	2.67E-03	3.15E-03	4.16E-04	13%
Muscle	2.93E-03	3.06E-03	2.47E-03	2.82E-03	3.10E-04	11%
Ovaries	3.53E-03	3.76E-03	2.93E-03	3.41E-03	4.29E-04	13%
Pancreas	1.53E-02	1.35E-02	1.01E-02	1.30E-02	2.64E-03	20%
Red marrow	4.65E-03	5.16E-03	3.58E-03	4.46E-03	8.06E-04	18%
Osteogenic cells	6.06E-03	6.67E-03	4.29E-03	5.67E-03	1.24E-03	22%
Skin	2.32E-03	2.45E-03	1.99E-03	2.25E-03	2.37E-04	11%
Spleen	3.45E-03	3.54E-03	2.76E-03	3.25E-03	4.27E-04	13%
Testes	NA	NA	2.36E-03	2.36E-03	NA	NA
Thymus	3.06E-03	3.16E-03	2.52E-03	2.91E-03	3.44E-04	12%
Thyroid	2.62E-03	2.81E-03	2.41E-03	2.61E-03	2.00E-04	8%
Urinary bladder wall	1.09E-02	1.51E-02	8.26E-03	1.14E-02	3.45E-03	30%
Uterus	3.63E-03	3.93E-03	3.06E-03	3.54E-03	4.42E-04	12%
Total body	3.61E-03	3.58E-03	2.83E-03	3.34E-03	4.42E-04	13%
Effective dose equivalent (mSv/MBq)	6.34E-03	6.20E-03	4.46E-03	5.67E-03	1.05E-03	18%
Effective dose (mSv/MBq)	4.96E-03	4.85E-03	3.58E-03	4.46E-03	7.67E-04	17%

COV = coefficient of variation; NA = not applicable.

activities from the total number of decays from 1 Bq of ^{11}C , assuming only physical decay.

$$\tilde{A}_{t_0 \rightarrow t_{\infty} \text{ remainder}} = 1 \text{ Bq} / \lambda_{\text{phys}} - \sum_{\text{organs}} \tilde{A}_{t_0 \rightarrow t_{\infty}} \quad \text{Eq. 5}$$

Absorbed Dose Estimation

Given the residence times, OLINDA 1.1 (48) was used to estimate the absorbed doses in adult phantoms. Absorbed dose per injected activity (mGy/MBq) was estimated for all organs of interest. The decays in the bladder were assumed to equal the decay-corrected whole-body fraction of injected activity in the bladder for the whole-body PET scan multiplied by τ , where $\tau = 1 \text{ Bq} / \lambda_{\text{phys}}$, 0.49 h

RESULTS

Safety and Biodistribution

Baseline ^{11}C -glutamine imaging data from 9 patients were evaluated. There were no signs of toxicity or observed adverse events after injection of ^{11}C -glutamine. Whole-body PET analysis in normal organs included evaluation of uptake in the salivary glands, heart, bladder, liver, spleen, kidneys, pancreas, stomach, small intestine, lungs, muscle, fat, brain, bone marrow, testis, and adrenals (Fig. 1; Supplemental Fig. 1; supplemental materials are available at <http://jnm.snmjournals.org>). The highest signal was observed in the bladder, as was expected because of excretion of the tracer. High activity was also seen in the pancreas and liver. Examination of the time-activity curves showed distinctive clearance profiles for different organs (Supplemental Fig. 2). High initial activity was seen in the kidneys (Supplemental Figs. 2A and 2B), spleen (Supplemental Fig. 2C), and heart (Supplemental Fig. 2D), with rapid clearance observed in all these organs. The liver showed a gradual increase in activity up to 5–15 min, followed by a slow washout (Supplemental Fig. 2E), whereas uptake in the pancreas increased up to 11–13 min and then plateaued (Supplemental Fig. 2F). There was low intestinal uptake, with activity peaking rapidly and then remaining stable up to the end of the dynamic scan (Supplemental Fig. 2G). Large variability was seen in the ^{11}C -glutamine time-activity curves for bone marrow in these patients (Supplemental Fig. 2H). There was variable uptake in the adrenals for

different patients, but all curves followed the same pattern (Supplemental Fig. 2I).

Estimated Absorbed Dose

The average number of decays per injected activity (Bq-h/Bq) for each organ is provided in Table 1. Table 2 provides the average absorbed dose per injected activity (mGy/MBq) for adults. The mean effective dose for ^{11}C -glutamine (\pm SD) was $4.46\text{E}-03 \pm 7.67\text{E}-04$ mSv/MBq. The organs with the highest doses were the liver ($1.68\text{E}-02 \pm 4.69\text{E}-03$ mGy/MBq), pancreas ($1.30\text{E}-02 \pm 2.64\text{E}-03$ mGy/MBq), and bladder wall ($1.14\text{E}-02 \pm 3.45\text{E}-03$ mGy/MBq). The only organ whose coefficient of variation was greater than 30% was the adrenal glands, at 35%.

Uptake in Metastatic Lesions

Accumulation of ^{11}C -glutamine exceeded the background level in several lesions across subjects presenting with pulmonary metastases (Figs. 2A, 2B, 3C, and 3D; Supplemental Fig. 3D) and hepatic metastases (Fig. 4C). Visualization of normal-organ accumulation in the whole-body images of a representative patient illustrating high uptake in the bladder, liver, and pancreas is shown in Figures 3A and 3B. ^{11}C -glutamine uptake in hepatic lesions was often at the periphery with a photopenic center, which existed on a high background of normal accumulation (Figs. 4A–4C). Some liver metastases and an adrenal mass were indistinguishable from background liver accumulation but could be imaged with an alternative tracer of glutamine metabolism (Supplemental Figs. 3A–3C and 4) (50,51). Skeletal metastases were also observed (Figs. 4A, 4B, and 4D). Interestingly, previously unidentified brain metastases were seen in 2 patients (Fig. 2C) and were subsequently confirmed using standard imaging (Fig. 2D). Glutamine-avid lesions typically exhibited rapid postinjection accumulation, which either plateaued or gradually decreased over time (Fig. 4E). Representative ^{11}C -glutamine tumor uptake values (lesion-to-blood pool ratios) are given in Table 3.

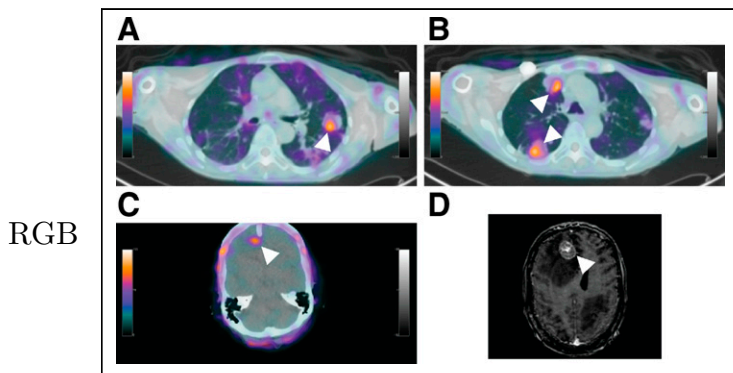


FIGURE 2. ^{11}C -glutamine tumor uptake in patient with metastatic colorectal cancer. (A–C) Axial ^{11}C -glutamine PET/CT images corresponding to left lung metastasis (A), 2 right lung metastases (B), and brain metastasis (C). Arrowheads point to lesions. Lesion-to-blood pool ratios from whole-body scan were 2.64 (A), 2.22 (B, top arrow), 2.35 (B, bottom arrow), and 1.68 (C). (D) Contrast-enhanced MRI 6.5 wk after baseline PET imaging and treatment. Lesion is indicated with arrowhead. MRI confirms presence of brain lesion seen with ^{11}C -glutamine PET.

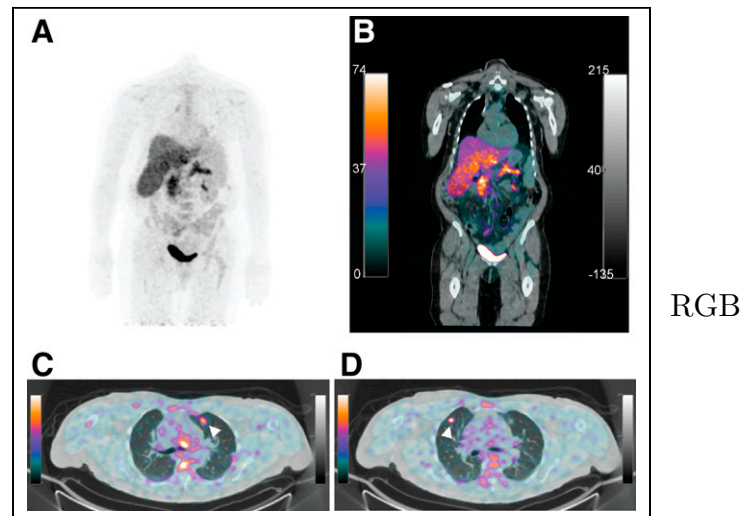


FIGURE 3. ^{11}C -glutamine biodistribution and tumor imaging in patient with metastatic colorectal cancer. (A and B) Whole-body PET (A) and PET/CT (B) images of ^{11}C -glutamine showing normal-organ accumulation. High uptake was seen in bladder, liver, and pancreas. (C and D) Axial ^{11}C -glutamine PET/CT fusion images corresponding to 2 lung nodules. Arrowheads point to lesions. Lesion-to-blood pool ratios from whole-body scan were 2.17 (C) and 2.59 (D).

RGB

RGB

DISCUSSION

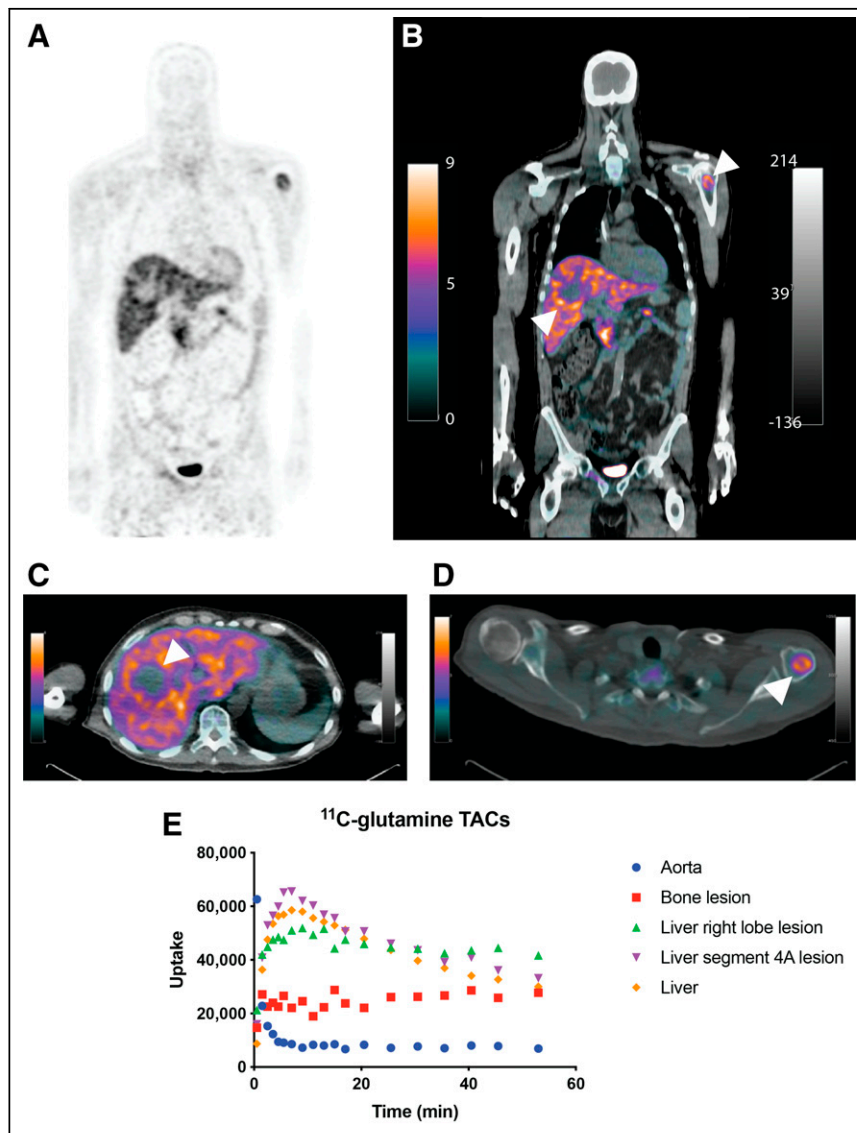
The role of altered metabolism in cancer progression is increasingly recognized (1,2). Altered glucose metabolism is a well-known phenomenon, but recently there has been growing emphasis on other pathways, including amino acid metabolism. As the most abundant amino acid in the plasma, glutamine has been shown to be vital to the growth and survival of certain cancers (3–9,11–14). Thus, glutaminolysis has emerged as a novel therapeutic target (3,4,7–9,11–14). However, methods to predict responders or monitor response to these new therapies are lacking. Novel imaging methods can be developed as biomarkers to meet this unmet need and aid in the pursuit of precision approaches to oncology. Previous studies have reported imaging with ^{11}C -labeled glutamine in preclinical models (21). Here, we present the clinical translation of this agent.

As part of this first-in-human study, we evaluated the safety and biodistribution of ^{11}C -glutamine in patients with metastatic colorectal cancer. ^{11}C -glutamine was found to be safe, with no adverse side effects observed at the dose used in this study. Uptake of ^{11}C -glutamine was highest in the bladder, liver, and pancreas. High uptake in the pancreas is consistent with previously reported biodistribution studies in mice (21). This uptake was attributed to the exocrine function and high protein turnover within the pancreas. Additionally, clearance profiles were comparable to those found in mice, with the heart and kidneys demonstrating rapid uptake and clearance but the liver showing a slower washout (21). Excretion through the bladder was also observed preclinically. The biodistribution pattern of ^{11}C -glutamine is consistent with the human biodistribution of another ^{11}C -labeled amino acid, L-[methyl- ^{11}C]methionine (52).

Use of ^{11}C -glutamine has several potential advantages, including the opportunity to leverage the short half-life of ^{11}C to follow other orthogonal metabolic pathways through simple sequential imaging protocols (51). Although certain technical advantages are inherent to the fluorinated agent, ^{18}F -(2S,4R)-4-fluoroglutamine, this tracer and ^{11}C -glutamine differ with respect to metabolic fate. For example, accumulated ^{18}F -(2S,4R)-4-fluoroglutamine remains as the parent compound, with a small fraction resulting from metabolites (28,31,34,40,43). Only a percentage is incorporated into biomolecules (28,29,34,38,40). An aliphatic fluoride-labeled analog, ^{18}F -(2S,4R)-4-fluoroglutamine is also prone to defluorination in vivo (28,31,37,38,40,43). In contrast, ^{11}C -glutamine is metabolized to ^{11}C -glutamate and ^{11}C - CO_2 (53), as well as incorporated directly into biomolecules (21). Generally, imaging with ^{11}C -glutamine reports on both uptake and downstream metabolism, whereas uptake of ^{18}F -(2S,4R)-4-

fluoroglutamine is likely more representative of glutamine transport (34). Thus, while ^{11}C -glutamine behaves identically to the naturally occurring substrate, this characteristic also represents a potential limitation of this tracer for PET imaging, as the signal detected will be from all radioactively labeled molecules, including the parent ligand and a range of metabolic intermediates.

The mean effective dose for ^{11}C -glutamine ($\pm\text{SD}$) was $4.46\text{E}-03 \pm 7.67\text{E}-04$ mSv/MBq. Although a full range of time points across the whole body were not collected in this study, our calculated value is comparable to other reported effective doses for ^{11}C -labeled PET tracers (52,54–57). This effective dose is similar to those reported for other ^{11}C -labeled amino acid radiopharmaceuticals (52,54,55) and a magnitude lower than dose estimates for ^{18}F -labeled radiopharmaceuticals found in the literature (50,58–62),



RGB

FIGURE 4. ^{11}C -glutamine biodistribution and tumor imaging in patient with metastatic colorectal cancer. (A and B) Whole-body PET (A) and PET/CT (B) images of ^{11}C -glutamine showing normal-organ accumulation and several metastases. High uptake was seen in bladder, liver, and pancreas. (C and D) Axial ^{11}C -glutamine PET/CT fusion images corresponding to liver metastasis (C) and left humeral head metastasis (D). Arrowheads point to lesions. Lesion-to-blood pool ratios from whole-body scan were 5.33 (C) and 4.02 (D). Lesion-to-liver ratio from whole-body scan was 1.66 (C). Time-activity curves (E) for aorta, liver, liver lesions, and bone metastasis.

TABLE 3
Quantification of ^{11}C -Glutamine Uptake in Tumors

Patient no.	Lesion location	Lesion-to-blood pool ratio*	Shown in ...
1	Right posterior hepatic lobe	5.40	Supplemental Fig. 3A
	Right adrenal	3.50	Supplemental Fig. 3C
	Lung LUL	2.17	Fig. 3C
	Liver segment 4A	5.11	Supplemental Fig. 3B
	Lung RUL	2.59	Fig. 3D
	Lung posterior LUL	1.93	Supplemental Fig. 3D
3	Bone T12	3.24	Not shown
	Liver right lobe	5.33	Fig. 4C
	Liver segment 4A	3.91	Not shown
	Bone left humeral head	4.02	Fig. 4D
8	Lung RLL	1.65	Not shown
	Lung LLL	2.54	Not shown
	Lung LUL	2.64	Fig. 2A
	Lung LUL	1.17	Not shown
	Lung RUL	2.22	Fig. 2B (top)
	Lung RLL	2.56	Not shown
	Brain	1.68	Fig. 2C
	Lung posterior RLL	2.35	Fig. 2B (bottom)

*Ratios of maximum value in lesion to average value in blood pool from whole-body images.
LUL = left upper lobe; RUL = right upper lobe; RLL = right lower lobe; LLL = left lower lobe.

due mainly to the short half-life of ^{11}C . This value compares well with the mean effective dose ($5.9\text{E}-03 \pm 2.0\text{E}-03$ mSv/MBq) reported in a review of 37 dose estimates for ^{11}C -labeled PET tracers (56) and with the average effective dose ($5.2\text{E}-03 \pm 1.7\text{E}-03$ mSv/MBq) from a recent review of 77 literature publications for a wide range of ^{11}C -labeled tracers (57). It is approximately one fourth the average effective dose ($2.05\text{E}-02 \pm 7.6\text{E}-03$ mSv/MBq) found from a review of 144 publications for a range of ^{18}F -labeled tracers (57). The effective dose estimate for ^{11}C -glutamine is about 4-fold less than that for ^{18}F -(2S,4R)-4-fluoroglutamine (42). Because the magnitudes of the SUVs of the 2 radiotracers are very similar (40), the difference in dosimetry can be attributed mainly to the difference in physical half-lives.

^{11}C -glutamine enabled the visualization of tumor lesions in various metastatic sites, including the liver, lungs, bones, and brain. Consistent with these data, prior human studies with ^{18}F -(2S,4R)-4-fluoroglutamine also showed tracer uptake in brain, bone, and lung metastases (40,41,43). Uptake of ^{18}F -(2S,4R)-4-fluoroglutamine in normal liver was more intense than that in liver lesions, with the tumor sites appearing as cold spots (41). This pattern matches the uptake pattern we observed for many of the liver lesions in our study using ^{11}C -glutamine. In hepatic metastases, normal-liver uptake can exceed tumor uptake, making it difficult to define tumor lesions. This characteristic represents a potential limitation of these tracers. A potential advantage of ^{11}C -glutamine could be in the detection of bone metastases, as these lesions could be missed with ^{18}F -(2S,4R)-4-fluoroglutamine because of normal uptake of free ^{18}F in the bone marrow through defluorination of the tracer (41). ^{18}F -(2S,4R)-4-fluoroglutamine enabled visualization of breast cancer lymph node metastases as well (36,42).

The utility of ^{11}C -glutamine in other cancer types was not evaluated in this work and will be the focus of future studies. Not all lesions identified in these patients were glutamine-avid. Thus, ^{11}C -glutamine PET may inform each metastatic tumor's underlying metabolism and biology. This intrapatient tumoral heterogeneity emphasizes the need for a noninvasive means of diagnosis and staging and points to the importance of using multiple orthogonal approaches to studying cancer. Imaging with ^{11}C -glutamine can complement other imaging approaches, including ^{18}F -FDG PET and PET imaging with other tracers currently in development, thus providing a more complete picture of the patient's disease and underlying biologic processes at individual metastatic sites. The use of total-body PET scanners could also potentially result in images with higher sensitivity for lesion detection and improved estimation of kinetic parameters by enabling simultaneous dynamic imaging of multiple organs or lesions (63–65). However, these scanners are still under development and not yet widely available.

One limitation of this study was the small sample size and evaluation within a focused clinical context (metastatic colorectal cancer). In addition, full quantitative analyses of tumor uptake were not performed. Thus, the diagnostic utility of ^{11}C -glutamine PET in colorectal cancer remains to be determined and is an area for future investigation. It is likely that other solid tumors may be effectively imaged with this tracer, which may also provide insight into tumors that may be sensitive to certain metabolically targeted therapies such as inhibitors of glutaminase activity (16) or glutamine transport (15). The utility of ^{11}C -glutamine PET in imaging tumors beyond colorectal cancer and in monitoring treatment response should be the focus of future work.

CONCLUSION

This clinical study demonstrated that ^{11}C -glutamine is well tolerated in humans. PET imaging with ^{11}C -glutamine is feasible, and elevated uptake was seen in lesions of patients with metastatic colorectal cancer. The estimated dosimetry is consistent with that of other ^{11}C -labeled tracers. Thus, further use of this tracer is warranted. Larger clinical studies will provide additional information and could demonstrate the utility of ^{11}C -glutamine for imaging in a variety of cancer types and for measurement of treatment response.

DISCLOSURE

This work was supported by grants from the NIH (P30 CA068485, P50 CA236733, U24 CA220325, R35 CA197570, S10 OD019963, and S10 OD012297) and generous philanthropic funding from the Julia Reed Foundation, Debbie and Michael Rose Discovery Grant, and Samuel K. and Sandra G. Wellborn Cancer Discovery Grant. H. Charles Manning is a Cancer Prevention Research Institute of Texas (CPRIT) Scholar in Cancer Research and is supported by CPRIT RR200046. No other potential conflict of interest relevant to this article was reported.

ACKNOWLEDGMENTS

We thank the patients and their families for participating in this study. Anna Fisher and Adam Rosenberg are acknowledged for experimental and manuscript support. The VUMC/VUIIS Human Imaging and Radiochemistry Core facilities assisted with PET and preparation of the radiotracer.

KEY POINTS

QUESTION: Is ^{11}C -glutamine safe and suitable for PET imaging of human cancer?

PERTINENT FINDINGS: In this study evaluating the safety and biodistribution of ^{11}C -glutamine and analyzing its ability to visualize metastatic lesions in patients with colorectal cancer, ^{11}C -glutamine was well tolerated and showed increased uptake in tumors relative to background.

IMPLICATIONS FOR PATIENT CARE: Imaging with ^{11}C -glutamine may advance precision medicine by enabling the characterization of tumors noninvasively by PET and may serve as a predictive and prognostic biomarker in future studies.

REFERENCES

- Hanahan D, Weinberg RA. Hallmarks of cancer: the next generation. *Cell*. 2011;144:646–674.
- Pavlova NN, Thompson CB. The emerging hallmarks of cancer metabolism. *Cell Metab*. 2016;23:27–47.
- Kishton RJ, Rathmell JC. Novel therapeutic targets of tumor metabolism. *Cancer J*. 2015;21:62–69.
- Sai KKS, Zachar Z, Bingham PM, Mintz A. Metabolic PET imaging in oncology. *AJR*. 2017;209:270–276.
- Pantel AR, Ackerman D, Lee SC, Mankoff DA, Gade TP. Imaging cancer metabolism: underlying biology and emerging strategies. *J Nucl Med*. 2018;59:1340–1349.
- DeBerardinis RJ, Cheng T. Q's next: the diverse functions of glutamine in metabolism, cell biology and cancer. *Oncogene*. 2010;29:313–324.
- Rajagopalan KN, DeBerardinis RJ. Role of glutamine in cancer: therapeutic and imaging implications. *J Nucl Med*. 2011;52:1005–1008.
- Choi YK, Park KG. Targeting glutamine metabolism for cancer treatment. *Biomol Ther (Seoul)*. 2018;26:19–28.
- Altman BJ, Stine ZE, Dang CV. From Krebs to clinic: glutamine metabolism to cancer therapy. *Nat Rev Cancer*. 2016;16:619–634.
- Sun A, Liu X, Tang G. Carbon-11 and fluorine-18 labeled amino acid tracers for positron emission tomography imaging of tumors. *Front Chem*. 2017;5:124.
- Zhu L, Ploessl K, Zhou R, Mankoff D, Kung HF. Metabolic imaging of glutamine in cancer. *J Nucl Med*. 2017;58:533–537.
- Scalise M, Pochini L, Galluccio M, Console L, Indiveri C. Glutamine transport and mitochondrial metabolism in cancer cell growth. *Front Oncol*. 2017;7:306.
- Liu Y, Zhao T, Li Z, Wang L, Yuan S, Sun L. The role of ASCT2 in cancer: a review. *Eur J Pharmacol*. 2018;837:81–87.
- Jiang H, Zhang N, Tang T, Feng F, Sun H, Qu W. Target the human alanine/serine/cysteine transporter 2 (ASCT2): achievement and future for novel cancer therapy. *Pharmacol Res*. 2020;158:104844.
- Schulte ML, Fu A, Zhao P, et al. Pharmacological blockade of ASCT2-dependent glutamine transport leads to antitumor efficacy in preclinical models. *Nat Med*. 2018;24:194–202.
- Cohen AS, Geng L, Zhao P, et al. Combined blockade of EGFR and glutamine metabolism in preclinical models of colorectal cancer. *Transl Oncol*. 2020;13:100828.
- Qu W, Zha Z, Ploessl K, et al. Synthesis of optically pure 4-fluoro-glutamines as potential metabolic imaging agents for tumors. *J Am Chem Soc*. 2011;133:1122–1133.
- Zhang X, Basuli F, Shi ZD, et al. Automated synthesis of [^{18}F](2S,4R)-4-fluoroglutamine on a GE TRACERlab FX-N Pro module. *Appl Radiat Isot*. 2016;112:110–114.
- Li S, Schmitz A, Lee H, Mach RH. Automation of the radiosynthesis of six different ^{18}F -labeled radiotracers on the AllinOne. *EJNMMI Radiopharm Chem*. 2017;1:15.
- Zhang Y, Zhang L, Yang J, et al. Initial experience in synthesis of (2S,4R)-4-[^{18}F]fluoroglutamine for clinical application. *J Labelled Comp Radiopharm*. 2019;62:209–214.
- Qu W, Oya S, Lieberman BP, et al. Preparation and characterization of L-[5- ^{11}C]-glutamine for metabolic imaging of tumors. *J Nucl Med*. 2012;53:98–105.
- Gleede T, Riehl B, Shea C, et al. Investigation of $\text{S}_{\text{N}}2$ [^{11}C]cyanation for base-sensitive substrates: an improved radiosynthesis of L-[5- ^{11}C]-glutamine. *Amino Acids*. 2015;47:525–533.
- Nasr K, Xin YC, Rydberg N, Hallgren R, Cai HC, Sun XK. Improved automated production for clinical use of C-11-L-glutamine [abstract]. *J Nucl Med*. 2017;58(suppl 1):872.
- Padakanti P, Schmitz A, Lee S, Mankoff D, Mach R. Synthesis of carbon-11 labelled L-glutamine on Synthra HCN synthesis module [abstract]. *J Nucl Med*. 2017;58(suppl 1):1025.
- Padakanti PK, Li S, Schmitz A, Mankoff D, Mach RH, Lee HS. Automated synthesis of [^{11}C]L-glutamine on Synthra HCN plus synthesis module. *EJNMMI Radiopharm Chem*. 2019;4:5.
- Rosenberg A, Nickels M, Schulte M, Manning HC. Automated clinical product of [^{11}C] glutamine on commercial synthesis modules [abstract]. *J Nucl Med*. 2017;58(suppl 1):332.
- Rosenberg AJ, Nickels ML, Schulte ML, Manning HC. Automated radiosynthesis of 5-[C-11]-glutamine, an important tracer for glutamine utilization. *Nucl Med Biol*. 2018;67:10–14.
- Lieberman BP, Ploessl K, Wang L, et al. PET imaging of glutaminolysis in tumors by ^{18}F -(2S,4R)-4-fluoroglutamine. *J Nucl Med*. 2011;52:1947–1955.
- Ploessl K, Wang L, Lieberman BP, Qu W, Kung HF. Comparative evaluation of ^{18}F -labeled glutamic acid and glutamine as tumor metabolic imaging agents. *J Nucl Med*. 2012;53:1616–1624.
- Wu Z, Zha Z, Li G, et al. [^{18}F](2S,4S)-4-(3-fluoropropyl)glutamine as a tumor imaging agent. *Mol Pharm*. 2014;11:3852–3866.
- Venneti S, Dunphy MP, Zhang H, et al. Glutamine-based PET imaging facilitates enhanced metabolic evaluation of gliomas in vivo. *Sci Transl Med*. 2015;7:274ra17.
- Hassanein M, Hight MR, Buck JR, et al. Preclinical evaluation of 4-[^{18}F]fluoroglutamine PET to assess ASCT2 expression in lung cancer. *Mol Imaging Biol*. 2016;18:18–23.
- Schulte ML, Hight MR, Ayers GD, et al. Non-invasive glutamine PET reflects pharmacological inhibition of BRAF(V600E) in vivo. *Mol Imaging Biol*. 2017;19:421–428.
- Zhou R, Pantel AR, Li S, et al. [^{18}F](2S,4R)-4-fluoroglutamine PET detects glutamine pool size changes in triple-negative breast cancer in response to glutaminase inhibition. *Cancer Res*. 2017;77:1476–1484.
- Abu Aboud O, Habib SL, Trott J, et al. Glutamine addiction in kidney cancer suppresses oxidative stress and can be exploited for real-time imaging. *Cancer Res*. 2017;77:6746–6758.
- Liu F, Xu X, Zhu H, et al. PET imaging of ^{18}F -(2S,4R)-4-fluoroglutamine accumulation in breast cancer: from xenografts to patients. *Mol Pharm*. 2018;15:3448–3455.
- Li C, Huang S, Guo J, et al. Metabolic evaluation of MYCN-amplified neuroblastoma by 4-[^{18}F]Fln PET imaging. *Mol Imaging Biol*. 2019;21:1117–1126.

38. Miner MW, Liljenback H, Virta J, et al. (2S, 4R)-4-[¹⁸F]fluoroglutamine for in vivo PET imaging of glioma xenografts in mice: an evaluation of multiple pharmacokinetic models. *Mol Imaging Biol.* 2020;22:969–978.
39. Viswanath V, Zhou R, Lee H, et al. Kinetic modeling of 18F-(2S,4R)-4-fluoroglutamine in mouse models of breast cancer to estimate glutamine pool size as an indicator of tumor glutamine metabolism. *J Nucl Med.* 2021;62:1154–1162.
40. Dunphy MPS, Harding JJ, Venneti S, et al. In vivo PET assay of tumor glutamine flux and metabolism: in-human trial of ¹⁸F-(2S,4R)-4-fluoroglutamine. *Radiology.* 2018;287:667–675.
41. Xu X, Zhu H, Liu F, et al. Imaging brain metastasis patients with ¹⁸F-(2S,4R)-4-fluoroglutamine. *Clin Nucl Med.* 2018;43:e392–e399.
42. Xu X, Zhu H, Liu F, et al. Dynamic PET/CT imaging of ¹⁸F-(2S, 4R)-4-fluoroglutamine in healthy volunteers and oncological patients. *Eur J Nucl Med Mol Imaging.* 2020;47:2280–2292.
43. Grkovski M, Goel R, Krebs S, et al. Pharmacokinetic assessment of ¹⁸F-(2S,4R)-4-fluoroglutamine in patients with cancer. *J Nucl Med.* 2020;61:357–366.
44. Shao A, Hathcock JN. Risk assessment for the amino acids taurine, L-glutamine and L-arginine. *Regul Toxicol Pharmacol.* 2008;50:376–399.
45. Ward E, Picton S, Reid U, et al. Oral glutamine in paediatric oncology patients: a dose finding study. *Eur J Clin Nutr.* 2003;57:31–36.
46. Ziegler TR, Benfell K, Smith RJ, et al. Safety and metabolic effects of L-glutamine administration in humans. *JPEN J Parenter Enteral Nutr.* 1990;14(suppl):137S–146S.
47. Stabin MG, Siegel JA. Physical models and dose factors for use in internal dose assessment. *Health Phys.* 2003;85:294–310.
48. Stabin MG, Sparks RB, Crowe E. OLINDA/EXM: the second-generation personal computer software for internal dose assessment in nuclear medicine. *J Nucl Med.* 2005;46:1023–1027.
49. ICRP. *Report of the Task Group on Reference Man: ICRP Publication 23.* Pergamon Press; 1975:235–237.
50. Smolarz K, Krause BJ, Graner FP, et al. (S)-4-(3-¹⁸F-fluoropropyl)-L-glutamic acid: an ¹⁸F-labeled tumor-specific probe for PET/CT imaging–dosimetry. *J Nucl Med.* 2013;54:861–866.
51. Kavanaugh G, Williams J, Morris AS, et al. Utility of [¹⁸F]FSPG PET to image hepatocellular carcinoma: first clinical evaluation in a US population. *Mol Imaging Biol.* 2016;18:924–934.
52. Deloar HM, Fujiwara T, Nakamura T, et al. Estimation of internal absorbed dose of L-[methyl-¹¹C]methionine using whole-body positron emission tomography. *Eur J Nucl Med.* 1998;25:629–633.
53. Padakanti P, Pantel AR, Choi H, et al. Refined analysis of [¹¹C]L-glutamine metabolism in triple negative breast cancer xenograft model. Digital poster presented at: World Molecular Imaging Conference; October 7–9, 2020; virtual.
54. Tolvanen T, Nagren K, Yu M, et al. Human radiation dosimetry of [¹¹C]MeAIB, a new tracer for imaging of system A amino acid transport. *Eur J Nucl Med Mol Imaging.* 2006;33:1178–1184.
55. Yao B, Tang C, Tang G, et al. Human biodistribution and radiation dosimetry of S-¹¹C-methyl-L-cysteine using whole-body PET. *Clin Nucl Med.* 2015;40:e470–e474.
56. van der Aart J, Hallett WA, Rabiner EA, Passchier J, Comley RA. Radiation dose estimates for carbon-11-labelled PET tracers. *Nucl Med Biol.* 2012;39:305–314.
57. Zanotti-Fregonara P, Lammertsma AA, Innis RB. ¹¹C dosimetry scans should be abandoned. *J Nucl Med.* 2021;62:158–159.
58. Deloar HM, Fujiwara T, Shidahara M, et al. Estimation of absorbed dose for 2-[F-18]fluoro-2-deoxy-D-glucose using whole-body positron emission tomography and magnetic resonance imaging. *Eur J Nucl Med.* 1998;25:565–574.
59. Graham MM, Peterson LM, Link JM, et al. Fluorine-18-fluoromisonidazole radiation dosimetry in imaging studies. *J Nucl Med.* 1997;38:1631–1636.
60. Vesselle H, Grierson J, Peterson LM, Muzi M, Mankoff DA, Krohn KA. ¹⁸F-fluorothymidine radiation dosimetry in human PET imaging studies. *J Nucl Med.* 2003;44:1482–1488.
61. Pauleit D, Floeth F, Herzog H, et al. Whole-body distribution and dosimetry of O-(2-[¹⁸F]fluoroethyl)-L-tyrosine. *Eur J Nucl Med Mol Imaging.* 2003;30:519–524.
62. Nye JA, Schuster DM, Yu W, Camp VM, Goodman MM, Votaw JR. Biodistribution and radiation dosimetry of the synthetic nonmetabolized amino acid analogue anti-¹⁸F-FACBC in humans. *J Nucl Med.* 2007;48:1017–1020.
63. Cherry SR, Badawi RD, Karp JS, Moses WW, Price P, Jones T. Total-body imaging: transforming the role of positron emission tomography. *Sci Transl Med.* 2017;9:eaa6169.
64. Badawi RD, Shi H, Hu P, et al. First human imaging studies with the EXPLORER total-body PET scanner. *J Nucl Med.* 2019;60:299–303.
65. Pantel AR, Viswanath V, Daube-Witherspoon ME, et al. PennPET Explorer: human imaging on a whole-body imager. *J Nucl Med.* 2020;61:144–151.